

1 **Observed influence of riming, temperature, and**  
2 **turbulence on the fallspeed of solid precipitation**

Timothy J. Garrett

3 Department of Atmospheric Sciences, University of Utah, Salt Lake City,  
4 USA

5 Sandra E. Yuter

6 Marine, Earth, and Atmospheric Sciences, North Carolina State University,  
7 Raleigh, USA

---

Department of Atmospheric Sciences, 135 S 1460 E, Rm 819, Salt Lake City, UT, 84103, USA  
(tim.garrett@utah.edu.)

8 Forecasts of the amount and geographic distribution of snow are highly  
9 sensitive to a model's parameterization of hydrometeor fallspeed. Riming is  
10 generally thought to lead to particles with a higher mass and terminal ve-  
11 locity. Yet models commonly assume that heavily rimed particles such as grau-  
12 pel have a fixed density and that their settling speed is unaffected by tur-  
13 bulence in storms. Here we show automated measurements of photographed  
14 hydrometeor shape and fallspeed using a new instrument placed in Utah's  
15 Wasatch Mountain Range. The data show that graupel in low turbulence con-  
16 ditions has a size-dependent fallspeed distribution with a mode near  $1 \text{ m s}^{-1}$ ,  
17 a result that is generally consistent with prior observations. However, the dis-  
18 tributions are broadened by turbulence and there is a correspondence be-  
19 tween particle density and air temperature. In high turbulence and at low  
20 temperatures, any sensitivity of fallspeed to particle size disappears.

## 1. Introduction

21 Solid precipitation is a critical component of any weather or climate model since predic-  
22 tions of precipitation amount, location and duration depend greatly on how precipitation  
23 particles are parameterized to grow and fall [*Rutledge and Hobbs*, 1984; *Lin et al.*, 1983;  
24 *Reisner et al.*, 1998; *Hong et al.*, 2004; *Garvert et al.*, 2005; *Colle et al.*, 2005; *Lin et al.*,  
25 2010; *Milbrandt et al.*, 2010; *Lin and Colle*, 2011; *Liu et al.*, 2011; *Iguchi et al.*, 2012;  
26 *Thériault et al.*, 2012b]. Unfortunately, few direct measurements of the fallspeed of solid  
27 precipitation have been made. Parameterizations that relate condensate amount to fall-  
28 speed [e.g. *Reisner et al.*, 1998; *Hong et al.*, 2004; *Tao et al.*, 2003] can often be traced to  
29 a single decades-old empirical study from the Cascade Mountain Range by *Locatelli and*  
30 *Hobbs* [1974] (LH74) that were based on just a few tens of data points per ice particle  
31 habit.

32 Greater generality has since been sought by considering hydrometeor fluid dynamics  
33 [*Böhm*, 1989; *Mitchell*, 1996; *Khvorostyanov and Curry*, 2002; *Heymsfield and Westbrook*,  
34 2010; *Kubicek and Wang*, 2012] or by using automated ground-based disdrometers orig-  
35 inally designed for sizing falling raindrops [*Kruger and Krajewski*, 2002; *Barthazy et al.*,  
36 2004; *Yuter et al.*, 2006; *Newman et al.*, 2009]. The results in either case are broadly con-  
37 sistent with LH74, yet the theoretical results assume the surrounding air is still rather than  
38 turbulent as would be normal in precipitating storms. Further, video disdrometers that  
39 obtain 200  $\mu\text{m}$  resolution silhouettes are subject to quantization and sizing errors [*Yuter*  
40 *et al.*, 2006; *Battaglia et al.*, 2010] and provide insufficient detail to quantify the extent of  
41 riming [*Barthazy and Schefold*, 2006; *Brandes et al.*, 2008]. Absent more comprehensive

42 measurements, model fall speed parameterizations are often tuned so that modeled pre-  
43 cipitation intensities and distributions in storms match observations [*Colle et al.*, 2005;  
44 *Lang et al.*, 2011].

45 This article presents an initial assessment of how riming and local meteorology affect  
46 frozen hydrometeor form, size, and fallspeed distributions using a combination of new  
47 measurements obtained at a high-altitude mountain field station in Utah. The centerpiece  
48 of the study is the newly developed Multi-Angle Snowflake Camera (MASC) [*Garrett et al.*,  
49 2012]. The MASC automatically photograph hydrometeors in freefall from multiple angles  
50 and at high resolution while simultaneously measuring their fallspeed.

## 2. Measurements

51 Between January and April of 2013, a suite of meteorological and microphysical instru-  
52 ments were deployed to the base of Alta Ski Area, located in Little Cottonwood Canyon  
53 in the Wasatch Mountain Range, Utah. Alta Base is at the bottom of Collins Gulch, a  
54 side canyon that rises from 2590 m above sea level to the Mt. Baldy summit at 3350 m.

55 At Alta Base, a MASC automatically photographed hydrometeors in freefall using three  
56 concentric cameras separated by  $36^\circ$ , each with a focal distance of 10 cm. As described in  
57 *Garrett et al.* [2012], two sets of near-infrared emitters and detectors, vertically separated  
58 by 32 mm, are used to calculate fallspeed and trigger photographs of hydrometeors larger  
59 than about 0.1 mm. The fallspeed is calculated from the time interval between two  
60 successive triggers, from top to bottom, provided they are within one second; i.e., the  
61 slowest measured fallspeed is  $0.03 \text{ m s}^{-1}$ . For this study, the camera exposure time was  
62  $1/25,000$ th of a second for the outer two 1.2 MP cameras with 16 mm and 12 mm lenses,

63 and 1/40,000th of a second for the center 5 MP camera with a 25 mm lens. The image  
64 resolutions were 26  $\mu\text{m}$ , 14  $\mu\text{m}$ , and 34  $\mu\text{m}$  with respective horizontal fields of view of 33  
65 mm, 33 mm and 44 mm. Triplet images of hydrometeors and associated fallspeeds were  
66 collected at a maximum rate of 2 Hz. Sizing errors associated with the placement of the  
67 hydrometeor within the depth of field are anticipated to be approximately 10%, although  
68 this error is constrained by multiple camera views.

69 Past measurements of hydrometeor fallspeeds have normally used a wind skirt or a  
70 funnel to still the air first. Recently, it has been found that this approach can lead  
71 to sampling biases depending on wind speed and hydrometeor habit and size [*Thériault*  
72 *et al.*, 2012a]. In this study, the MASC was intentionally exposed so that it measured the  
73 hydrometeor fallspeed  $v$  instead of the terminal velocity  $v_T$ .

74 The MASC was co-located with a vertically-pointing METEK 24.1 GHz MicroRain-  
75 Radar [*Löffler-Mang et al.*, 1999; *Peters et al.*, 2002]. The MRR data are post-processed  
76 to improve data quality and sensitivity using the method of *Maahn and Kollias* [2012].  
77 The minimum detectable echo is approximately -5 dBZ. The MRR obtains a vertical  
78 profile every 30 seconds up to 4.8 km AGL with thirty-two 150 m deep range gates.  
79 Measurements of snowfall, windspeed, temperature and relative humidity were obtained  
80 throughout Collins Gulch. Here the focus is on temperatures at Mt. Baldy summit  $T_{Baldy}$   
81 and Alta Base  $T_{Base}$ . The respective means and standard deviations during snow events  
82 were  $-10.0 \pm 4.9^\circ\text{C}$  and  $-3.6 \pm 4.3^\circ\text{C}$ .

## 2.1. Effect of riming on size distributions and fallspeed

A subset of 35687 hydrometeors was obtained during winter 2013 that satisfied stringent image selection criteria that eliminated focus or coincidence errors that might lead to erroneous fallspeed associations. Prior studies have identified particle form from the ratio of a silhouette’s perimeter  $P$  to its cross-section [Lindqvist *et al.*, 2012; Schmitt and Heymsfield, 2014]. An advantage of MASC photographs is that particles are photographed from three angles. Additional shape information can be derived from the mean inter-pixel brightness variability  $\langle\sigma\rangle$  within each image cross-section [Nurzynska *et al.*, 2012]. The particle complexity  $\chi$  is defined as

$$\chi = \frac{P}{2\pi r_{eq}} (1 + \langle\sigma\rangle) \quad (1)$$

83 where  $r_{eq}$  is the area equivalent radius of the photographed particle cross-section and  $\chi$  is  
 84 averaged over triplet views. A value of  $\chi = 1$  translates to a perfect, homogenous circle.

85 The complexity metric offers an objective measure for batch-processing of hydrometeor  
 86 type. Riming tends to “round” and “smooth” hydrometeors leading to relatively low  
 87 values of  $\chi$ . Classification boundaries are always somewhat subjective. A randomly chosen  
 88 selection of images shown in Figure 1 illustrates how values of  $\chi$  less than 1.35 consistently  
 89 correspond with lump and conical graupel. More aggregated forms have values greater  
 90 than 1.75. Heavily rimed crystals and aggregates tend to lie in between.

91 If riming extent is categorized according to complexity  $\chi$  (Table 1) then, on average, our  
 92 observations show that increased riming corresponds with more compact and faster falling  
 93 particles that form under higher temperatures with higher values of column-integrated  
 94 Doppler spectral width and Doppler velocity. The meteorological contrasts are surpris-

95 ingly small given the sharper contrasts between graupel and aggregate form. For example,  
96 the average Mt. Baldy temperature associated with aggregates is  $-10.6^{\circ}\text{C}$ , compared with  
97  $-8.4^{\circ}\text{C}$  for graupel; the respective average radar echo depths are 1.40 km and 1.23 km.

98 Fig. 2 shows that riming corresponds with more compact particles that have higher  
99 mode and maximum fallspeeds. Normalized size distributions of the particles generally  
100 take the form of a gamma function. Looking at the slope of the tail of the distribution  
101  $\lambda$  (e.g.  $N(D_{max}) = N_0 \exp(-\lambda D_{max})$ ), values range from  $0.69\text{ mm}^{-1}$  for aggregates to  
102  $1.99\text{ mm}^{-1}$  for graupel. The slope values are generally consistent with prior observations,  
103 although the value for aggregates is lower than the minimum value of  $0.9\text{ mm}^{-1}$  that  
104 has sometimes been considered possible for generic “snow” [Braham, 1990]. It has been  
105 suggested that the earlier size distribution measurements may have been steepened by  
106 artifacts produced during airborne sampling [Heymsfield et al., 2008].

107 The relationship between fallspeed and degree of riming in Fig. 2 is qualitatively con-  
108 sistent with the results of LH74 who found that aggregates generally fall more slowly than  
109 graupel (Table 1). Here the average fallspeed of graupel is  $0.90\text{ m s}^{-1}$  compared to  $0.72\text{ m}$   
110  $\text{s}^{-1}$  for aggregates. What is unusual is that slightly more than one half of each fallspeed  
111 distribution had values lower than  $0.5\text{ m s}^{-1}$ . In contrast, LH74 observed no graupel that  
112 fell slower than  $0.8\text{ m s}^{-1}$  and no aggregates that fell slower than  $0.5\text{ m s}^{-1}$ .

## 2.2. The effect of size, turbulence, and temperature on fallspeed

113 What controls the measured fallspeed distributions? The terminal velocity  $v_T$  in still  
114 air of a given density is determined by particle density, shape, and size [Böhm, 1989].

115 However, because air is turbulent and snowflakes are efficient tracers of atmospheric eddies  
 116 [*Toloui et al.*, 2014], the terminal velocity may differ from the actual fallspeed  $v$ .

117 To examine this issue more closely, the focus here is on graupel. Graupel is compara-  
 118 tively spherical relative to more complex particle types. Its physical boundaries can be  
 119 more easily constrained using MASC multi-angle images. To determine the relationships  
 120 between density, size, turbulence and fallspeed, fluid dynamical calculations are made  
 121 considering particle size, shape, and orientation using expressions from *Böhm* [1989]. The  
 122 terminal velocity in still air can be related to a modified Davies number that is a func-  
 123 tion of the local air density, the circumscribing area projected normal to the vertical  
 124  $A_{max}$ , the particle cross-section  $A$ , and the particle mass. The area equivalent radius is  
 125  $r_{eq} = \sqrt{(A/\pi)}$  and a mass estimate is  $m = 4\pi\rho r_{eq}^3/3$ .

126 Using the *Böhm* [1989] expressions, two approaches are taken. The first is to calculate  
 127 the terminal velocity  $v_T$  based on a graupel particle’s observed size and shape and an as-  
 128 sumed “medium” graupel density  $\rho_g^{medium}$  of  $400 \text{ kg/m}^3$  that is commonly used in weather  
 129 models [e.g. *Rutledge and Hobbs*, 1984; *Meyers et al.*, 1997; *Thompson et al.*, 2004; *Seifert*  
 130 *and Beheng*, 2006]. The second is to do the inverse and infer an aerodynamic “effective  
 131 density”  $\rho_g^{aer}(v)$  by assuming that the measured fallspeed  $v$  in turbulent air is equivalent  
 132 to the terminal velocity  $v_T$  that is appropriate for still air.

133 Taking the first approach, the calculated average value of  $v_T$  is  $2.3 \text{ m s}^{-1}$ , which is more  
 134 than twice as fast as the average graupel fallspeed that was directly measured (Table 1).  
 135 Taking the second approach, the average value of  $\rho_g^{aer}$  is  $215 \text{ kg m}^{-3}$ , or about one half



136 of  $\rho_g^{medium}$ . The implication is that  $\rho_g^{medium}$  may be an overestimate, at least for high  
137 elevation conditions similar to those at Alta.

138 LH74 used manual techniques to estimate values for graupel density that lay between 50  
139  $\text{kg m}^{-3}$  and  $450 \text{ kg m}^{-3}$ . While the average values of  $\rho_g^{aer}$  from Alta lie within this range,  
140 the range of measured fallspeeds shown in Fig. 2 is so broad as to imply that a large  
141 fraction of graupel particles had very small values of  $\rho_g^{aer}$ . In fact, the subset of graupel  
142 with fallspeeds below  $0.5 \text{ m s}^{-1}$  had an average value of  $\rho_g^{aer}$  of just  $5.6 \text{ kg m}^{-3}$ . If this  
143 were indeed the physical density  $\rho_g$ , it would seem somewhat implausible since it would  
144 imply that air made up more than 99% of each particle. Otherwise, graupel particles in  
145 the  $v < 0.5 \text{ m s}^{-1}$  and  $v > 0.5 \text{ m s}^{-1}$  mode fall speed modes had effectively identical  
146 values of the average complexity (1.18) and maximum dimension (1.43 mm). Alta Base  
147 temperatures were identical as well ( $-2^\circ \text{ C}$ ).

148 The alternative explanation is that  $\rho_g^{aer}$  does not represent the true physical density  
149 because the measured fallspeed does not always equal the terminal velocity. To exam-  
150 ine the extent to which fallspeed is determined by physical rather than aerodynamic  
151 considerations, graupel fallspeed distributions are grouped according to temperature and  
152 turbulence, with nominal low and high values defined by the lower and upper quartiles in  
153 the total dataset.

154 Temperature measurements from Mt. Baldy are used here rather than those from Alta  
155 Base since these are the values that are assumed to be closer to the conditions aloft where  
156 the graupel formed [Steenburgh and Alcott, 2008]. No direct in situ measurement of tur-  
157 bulence was made. Instead, an estimate can be derived from the difference between the

158 maximum wind speed, or gust that was sampled every 3 sec, and the average wind speed,  
159 as determined from successive 5 min intervals at Alta Base. Following *Schreur and Geert-*  
160 *sema* [2008], estimated turbulence is proportional to  $E = (\text{Gusts} - \text{Average Wind})^2/2$ .

161 Graupel and meteorological properties separated by temperature and turbulence quar-  
162 tiles are summarized in Table 2. Temperatures higher than  $-5\text{ }^\circ\text{C}$  (average  $-3.5\text{ }^\circ\text{C}$ ) at Mt.  
163 Baldy were associated with a mean fallspeed of  $1.16\text{ m s}^{-1}$  compared with  $0.70\text{ m s}^{-1}$  when  
164 the temperatures were lower than  $-13\text{ }^\circ\text{C}$  (average  $-17.3\text{ }^\circ\text{C}$ ). The mean aerodynamically  
165 derived densities for the high temperature and low temperature quartiles were  $217\text{ kg m}^{-3}$   
166 and  $159\text{ kg m}^{-3}$ , respectively, while the average particle sizes were statistically equivalent.  
167 The implication is that graupel that formed at higher temperatures fell faster because it  
168 was more dense.

169 Between the low ( $0.2\text{ m}^2\text{ s}^{-2}$ ) and high ( $8.1\text{ m}^2\text{ s}^{-2}$ ) turbulence quartiles summarized  
170 in Table 2, the average Mt. Baldy temperatures and MASC measured fallspeeds were  
171 similar. However, with the higher values of  $E$ , the median fallspeed shifted from  $0.68$  to  
172  $0.33\text{ m s}^{-1}$ ; average values of  $D_{max}$  remained unchanged.

173 Turbulence measured near the MASC tended to extend throughout the column. The  
174 column averaged Doppler spectral width (SW) obtained from the MRR provides a proxy  
175 measurement of turbulence further aloft [*Wakasugi et al.*, 1986; *Rinehart*, 2004]. Average  
176 values of SW were 60% higher in the upper quartile of  $E$  than in the lower quartile.  
177 Time-height profiles of MRR SW (not shown) indicate that higher SW values that can  
178 occur near the surface can also occur at mid-levels in the radar echo.

179 Figure 3 shows normalized distributions for graupel fallspeed as a function of  $D_{max}$ ,  
180 separated according to the aforementioned temperature and turbulence quartiles. LH74  
181  $v_T(D_{max})$  power-law relations for lump and conical graupel are superimposed for compar-  
182 ison. The range of values of  $v(D_{max})$  observed by the MASC are comparatively broad,  
183 with an overall bias towards lower values.

184 Nonetheless, there is a weak similarity between the results presented here and those of  
185 LH74, especially when temperatures are high and turbulence is low. For these conditions,  
186 there is a similar fallspeed mode near  $1 \text{ m s}^{-1}$  and also evidence of a linear correlation  
187 between  $\log v$  and  $\log D_{max}$ . In particular, when turbulence is low, the  $v < 0.5 \text{ m s}^{-1}$   
188 mode shown in Fig. 2 is much less pronounced. When turbulence is high, however,  
189 fallspeeds broaden to both lower and higher values, the  $v < 0.5 \text{ m s}^{-1}$  mode becomes  
190 more pronounced, and there is no apparent power-law relationship between fallspeed and  
191 size ( $r = -0.05$ ). At low temperatures, fallspeeds are generally slower, and the power-law  
192 relationship is also no longer evident ( $r = 0.06$ ).

### 3. Discussion

193 Even to the most casual observer it is readily apparent that snow swirls, even in light  
194 winds. In fact, *Toloui et al.* [2014] have found that falling snowflakes can be used as fluid  
195 tracers to accurately derive turbulent energy spectra for air. The measurements presented  
196 here also seem to indicate that the average fallspeed of hydrometeors is determined by  
197 turbulence, in addition to particle size and shape.

198 Studies of the inertial response of particles to turbulence often make a distinction be-  
199 tween terminal velocity and the average fallspeed or settling speed  $W$  [*Wang and Maxey,*

1993; *Nielsen*, 1993]. With “sweeping”, falling particles are accelerated by the downward motions of eddies. “Loitering” buoys faster falling particles in the eddy upward motions. Recent wind tunnel studies by *Good et al.* [2012] point to a continuum in  $W/v_T$  with respect to a large-scale settling parameter  $v_T/v_{rms}$ , where  $v_{rms}$  is the root mean squared vertical velocity of the turbulent flow. Sweeping dominates when  $v_T/v_{rms}$  is less than about 0.1, in which case  $W$  is determined more by  $v_{rms}$  than  $v_T$ . Otherwise, loitering limits  $W$  to as little as one fifth of  $v_T$ .

Unfortunately, no measurement of  $v_{rms}$  was made adjacent to the MASC that could have been used to directly quantify the level of turbulence. Using nearby wind speeds and gusts as a proxy, the results shown in Figure 3 strongly suggest that turbulence broadens measured fallspeed distributions through both loitering and sweeping. In fact, it erased any sensitivity of fallspeed to particle size that might be attributed to the terminal velocity. This suggests that turbulent eddies played an important if not dominant role in determining the nature of the fallspeed distribution.

As a caveat, it could be that the MASC body disturbed the fallspeed measurements in the presence of high winds, and this will be investigated in the future. Nonetheless, we observed a surprisingly broad range of graupel fallspeeds, even in the very stillest air sampled at Alta. Average wind speeds near the MASC in the low  $E$  quartile shown in Fig 3 were just  $1.2 \text{ m s}^{-1}$ . Even so, 25% of graupel had fallspeeds less than  $0.17 \text{ m s}^{-1}$  and 25% had fallspeeds greater than  $1.25 \text{ m s}^{-1}$ .

Temperature appears to influence fallspeed more indirectly through its effect on particle density. Wind tunnel studies show that graupel density  $\rho_g$  can be related to the impaction

222 speed  $v_i$  (m/s) of accreted droplets of radius  $r$  ( $\mu\text{m}$ ) on a surface with temperature  $T_S$  ( $^{\circ}\text{C}$ )  
223 through  $\rho_g \propto (-rv_i/T_s)^\alpha$ , where  $\alpha$  is a constant [Macklin, 1962; Pflaum and Pruppacher,  
224 1979; Heymsfield and Pflaum, 1985; Rasmussen and Heymsfield, 1985; Prodi et al., 1986;  
225 Cober and List, 1993]. Macklin [1962] hypothesized that low temperatures and impaction  
226 at slow speeds leads to a porous rime. Faster impaction at higher temperature allows liquid  
227 to fill any gaps in the rimed structure before freezing to form higher density accretions.

228 At Alta, we found that a change in  $T_{Baldy}$  from  $-3.5^{\circ}\text{C}$  to  $-17.3^{\circ}\text{C}$  was associated with  
229 a 37% reduction in the mean value of the effective density  $\rho_g^{aer}$  (Table 2). Milbrandt and  
230 Morrison [2013] have shown numerically that this relationship between temperature and  
231 graupel density introduces an important positive feedback: as graupel falls through higher  
232 temperatures, it becomes denser and falls ever faster. This permits solid precipitation that  
233 forms within the strong updrafts of a squall line to reach to the surface without requiring  
234 a separate model category for hail .

#### 4. Summary

235 Data from a new instrument that takes high speed multi-angle photographs of hydrom-  
236 eteors in freefall confirms previous work that graupel is more compact and falls faster than  
237 aggregates or more lightly rimed particles. A large sample size of simultaneous particle  
238 size and fall speed measurements, placed in the context of observations of temperature  
239 and turbulence, suggests several refinements to our understanding of the physical charac-  
240 teristics of graupel. An effective density was calculated for graupel based on aerodynamic  
241 considerations that is about half the value of  $400 \text{ kg m}^{-3}$  that is commonly assumed in  
242 weather models. Further, the data suggest that graupel formed at lower temperatures is

243 less dense. Strong turbulence broadens the distribution of fallspeeds to the point that the  
244 signature relationship of terminal velocity to particle size is no longer evident.

245 **Acknowledgments.** This work was supported by the National Science Foundation,  
246 Award No. ATM- 1127692. Cale Fallgatter, Konstantin Shkurko, Daniel Howlett, Spencer  
247 Rhodes, the Center for Snow Science at Alta, and Alta Ski Area contributed to the  
248 instrument development, field operations, and data analysis. The datasets used for this  
249 study are archived at <http://content.lib.utah.edu/cdm/ref/collection/uspace/id/10605>

## References

- 250 Barthazy, E., and R. Schefold, Fall velocity of snowflakes of different riming degree and  
251 crystal types, *Atmos. Res.*, *82*, 391–398, 2006.
- 252 Barthazy, E., S. Göke, R. Schefold, and D. Högl, An optical array instrument for shape  
253 and fall velocity measurements of hydrometeors, *J. Atmos. Oceanic. Technol.*, *21*, 1400–  
254 +, doi:10.1175/1520-0426(2004)021, 2004.
- 255 Battaglia, A., E. Rustemeier, A. Tokay, U. Blahak, and C. Simmer, Parsivel snow ob-  
256 servations: A critical assessment, *J. Atmos. Oceanic Technol.*, *27*(2), 333–344, doi:  
257 10.1175/2009JTECHA1332.1, 2010.
- 258 Böhm, H. P., A general equation for the terminal fall speed of solid hydrometeors., *J.*  
259 *Atmos. Sci.*, *46*, 2419–2427, doi:10.1175/1520-0469(1989)046;2419:AGEFTT;2.0.CO;2,  
260 1989.
- 261 Braham, R. R., Snow particle size spectra in lake effect snows, *J. Appl. Meteor.*, *29*(3),  
262 200–207, doi:10.1175/1520-0450(1990)029;0200:SPSSIL;2.0.CO;2, 1990.

- 263 Brandes, E. A., K. Ikeda, G. Thompson, and M. Schönhuber, Aggregate termi-  
264 nal velocity/temperature relations, *J. Appl. Meteorol. Clim.*, *47*, 2729–2736, doi:  
265 10.1175/2008JAMC1869.1, 2008.
- 266 Cober, S. G., and R. List, Measurements of the heat and mass transfer parameters char-  
267 acterizing conical graupel growth, *J. Atmos. Sci.*, *50*(11), 1591–1609, doi:10.1175/1520-  
268 0469(1993)050;1591:MOTHAM;2.0.CO;2, 1993.
- 269 Colle, B. A., M. F. Garvert, J. B. Wolfe, C. F. Mass, and C. P. Woods, The 13 14  
270 December 2001 IMPROVE-2 Event. Part III: Simulated Microphysical Budgets and  
271 Sensitivity Studies., *J. Atmos. Sci.*, *62*, 3535–3558, doi:10.1175/JAS3552.1, 2005.
- 272 Garrett, T. J., C. Fallgatter, K. Shkurko, and D. Howlett, Fall speed measurement and  
273 high-resolution multi-angle photography of hydrometeors in free fall, *Atmospheric Mea-  
274 surement Techniques*, *5*(11), 2625–2633, doi:10.5194/amt-5-2625-2012, 2012.
- 275 Garvert, M. F., C. P. Woods, B. A. Colle, C. F. Mass, P. V. Hobbs, M. T. Stoelinga,  
276 and J. B. Wolfe, The 13 14 December 2001 IMPROVE-2 Event. Part II: Comparisons  
277 of MM5 Model Simulations of Clouds and Precipitation with Observations., *Journal of  
278 Atmospheric Sciences*, *62*, 3520–3534, doi:10.1175/JAS3551.1, 2005.
- 279 Good, G. H., S. Gerashchenko, and Z. Warhaft, Intermittency and inertial particle en-  
280 trainment at a turbulent interface: the effect of the large-scale eddies, *J. Fluid Mech.*,  
281 *694*, 371–398, doi:10.1017/jfm.2011.552, 2012.
- 282 Heymsfield, A. J., and J. C. Pflaum, A quantitative assessment of the accuracy of  
283 techniques for calculating graupel growth, *J. Atmos. Sci.*, *42*(21), 2264–2274, doi:  
284 10.1175/1520-0469(1985)042;2264:AQAOTA;2.0.CO;2, 1985.

- 285 Heymsfield, A. J., and C. D. Westbrook, Advances in the estimation of ice particle fall  
286 speeds using laboratory and field measurements, *J. Atmos. Sci.*, *67*, 2469–2482, doi:  
287 10.1175/2010JAS3379.1, 2010.
- 288 Heymsfield, A. J., P. Field, and A. Bansemer, Exponential size distributions for snows, *J.*  
289 *Atmos. Sci.*, *65*(12), 4017–4031, doi:10.1175/2008JAS2583.1, 2008.
- 290 Hong, S., J. Dudhia, and S. Chen, A revised approach to ice microphysical processes for  
291 the bulk parameterization of clouds and precipitation, *Mon. Wea. Rev.*, *132*, 103–120,  
292 doi:10.1175/1520-0493(2004)132;0103:ARATIM;2.0.CO;2, 2004.
- 293 Iguchi, T., T. Matsui, J. J. Shi, W.-K. Tao, A. P. Khain, A. Hou, R. Cifelli, A. Heyms-  
294 field, and A. Tokay, Numerical analysis using WRF-SBM for the cloud microphys-  
295 ical structures in the C3VP field campaign: Impacts of supercooled droplets and  
296 resultant riming on snow microphysics, *J. Geophys. Res.*, *117*(D23), D23,206, doi:  
297 10.1029/2012JD018101, 2012.
- 298 Khvorostyanov, V. I., and J. A. Curry, Terminal velocities of droplets and crystals: Power  
299 laws with continuous parameters over the size spectrum, *J. Atmos. Sci.*, *59*, 1872–1884,  
300 doi:10.1175/1520-0469(2002)059;1872:TVODAC;2.0.CO;2, 2002.
- 301 Kruger, A., and W. F. Krajewski, Two-dimensional video disdrometer: A description, *J.*  
302 *Atmos. Oceanic. Technol.*, *19*, 602–617, 2002.
- 303 Kubicek, A., and P. K. Wang, A numerical study of the flow fields around a typical  
304 conical graupel falling at various inclination angles, *Atmospheric Research*, *118*(0), 15  
305 – 26, doi:10.1016/j.atmosres.2012.06.001, 2012.



- 306 Lang, S. E., W.-K. Tao, X. Zeng, and Y. Li, Reducing the biases in simulated radar  
307 reflectivities from a bulk microphysics scheme: Tropical convective systems., *J. Atmos.*  
308 *Sci.*, *68*(10), 2306–2320, 2011.
- 309 Lin, Y., and B. A. Colle, A new bulk microphysical scheme that includes riming intensity  
310 and temperature dependent ice characteristics, *Mon. Wea. Rev.*, *139*, 1013–1035, doi:  
311 dx.doi.org/10.1175/2010MWR3293.1, in press, 2011.
- 312 Lin, Y., L. J. Donner, and B. A. Colle, Parameterization of riming intensity and its  
313 impact on ice fall speed using arm data, *Mon. Wea. Rev.*, *139*(3), 1036–1047, doi:  
314 10.1175/2010MWR3299.1, 2010.
- 315 Lin, Y. L., R. D. Farley, and H. D. Orville, Bulk parameterization of the snow field in a  
316 cloud model, *J. Clim. Appl. Meteor.*, *22*, 1065–1092, 1983.
- 317 Lindqvist, H., K. Muinonen, T. Nousiainen, J. Um, G. M. McFarquhar, P. Haapanala,  
318 R. Makkonen, and H. Hakkarainen, Ice-cloud particle habit classification using principal  
319 components, *J. Geophys. Res.*, *117*, D16206, doi:10.1029/2012JD017573, 2012.
- 320 Liu, C., K. Ikeda, G. Thompson, R. Rasmussen, and J. Dudhia, High-resolution sim-  
321 ulations of wintertime precipitation in the colorado headwaters region: Sensitivity to  
322 physics parameterizations., *Monthly Weather Review*, *139*(11), 3533 – 3553, 2011.
- 323 Locatelli, J. D., and P. V. Hobbs, Fall speeds and masses of solid precipitation particles,  
324 *J. Geophys. Res.*, *79*, 2185–2197, doi:10.1029/JC079i015p02185, 1974.
- 325 Löffler-Mang, M., M. Kunz, and W. Schmid, On the performance of a low-cost K-band  
326 doppler radar for quantitative rain measurements, *J. Atmos. and Ocean. Tech.*, *16*,  
327 379–387, doi:10.1175/1520-0426(1999)016<0379:OTPOAL>2.0.CO;2, 1999.

- 328 Maahn, M., and P. Kollias, Improved micro rain radar snow measurements using doppler  
329 spectra post-processing, *Atmospheric Measurement Techniques*, 5(11), 2661–2673, 2012.
- 330 Macklin, W. C., The density and structure of ice formed by accretion, *Q. J. Roy. Meteorol.*  
331 *Soc.*, 88(375), 30–50, doi:10.1002/qj.49708837504, 1962.
- 332 Meyers, M. P., R. L. Walko, J. Y. Harrington, and W. R. Cotton, New {RAMS} cloud  
333 microphysics parameterization. part ii: The two-moment scheme, *Atmos. Res.*, 45(1),  
334 3 – 39, doi:http://dx.doi.org/10.1016/S0169-8095(97)00018-5, 1997.
- 335 Milbrandt, J. A., and H. Morrison, Prediction of graupel density in a bulk microphysics  
336 scheme., *J. Atmos. Sci.*, 70(2), 410 – 429, 2013.
- 337 Milbrandt, J. A., M. K. Yau, J. Mailhot, S. Bélair, and R. McTaggart-Cowan, Simulation  
338 of an Orographic Precipitation Event during IMPROVE-2. Part II: Sensitivity to the  
339 Number of Moments in the Bulk Microphysics Scheme, *Mon. Wea. Rev.*, 138, 625–642,  
340 doi:10.1175/2009MWR3121.1, 2010.
- 341 Mitchell, D. L., Use of mass- and area-dimensional power laws for determining precip-  
342 itation particle terminal velocities., *J. Atmos. Sci.*, 53, 1710–1723, doi:10.1175/1520-  
343 0469(1996)053, 1996.
- 344 Newman, A. J., P. A. Kucera, and L. F. Bliven, Presenting the Snowflake Video Im-  
345 ager (SVI), *J. Atmos. Oceanic. Technol.*, 26, 167–179, doi:10.1175/2008JTECHA1148.1,  
346 2009.
- 347 Nielsen, P., Turbulence effects on the settling of suspended particles, *J. Sedim. Petrol.*,  
348 63, 835–838, 1993.

- 349 Nurzyska, K., M. Kubo, and K. ichiro Muramoto, Texture operator for snow parti-  
350 cle classification into snowflake and graupel, *Atmos. Res.*, *118*(0), 121 – 132, doi:  
351 10.1016/j.atmosres.2012.06.013, 2012.
- 352 Peters, G., B. Fischer, and T. Andersson, Rain observations with a vertically looking  
353 Micro Rain Radar (MRR), *Boreal Environ. Res.*, *7*, 353–362, 2002.
- 354 Pflaum, J. C., and H. R. Pruppacher, A wind tunnel investigation of the growth of  
355 graupel initiated from frozen drops, *J. Atmos. Sci.*, *36*(4), 680–689, doi:10.1175/1520-  
356 0469(1979)036;0680:AWTIOT;2.0.CO;2, 1979.
- 357 Prodi, F., L. Levi, and P. Pederzoli, The density of accreted ice, *Q. J. Roy. Meteorol.*  
358 *Soc.*, *112*(474), 1081–1090, doi:10.1002/qj.49711247409, 1986.
- 359 Rasmussen, R. M., and A. J. Heymsfield, A generalized form for impact velocities used  
360 to determine graupel accretional densities, *J. Atmos. Sci.*, *42*(21), 2275–2279, doi:  
361 10.1175/1520-0469(1985)042;2275:AGFFIV;2.0.CO;2, 1985.
- 362 Reisner, J., R. M. Rasmussen, and R. T. Bruintjes, Explicit forecasting of supercooled  
363 liquid water in winter storms using the MM5 mesoscale model, *Q. J. Roy. Meteorol.*  
364 *Soc.*, *124*, 1071–1107, doi:10.1256/smsqj.54803, 1998.
- 365 Rinehart, R., A solution of the problem of rapid scanning for radar antennae, *Journal of*  
366 *Applied Physics*, *19*(9), 860–862, 2004.
- 367 Rutledge, S. A., and P. V. Hobbs, The Mesoscale and Microscale Structure and Organiza-  
368 tion of Clouds and Precipitation in Midlatitude Cyclones. XII: A Diagnostic Modeling  
369 Study of Precipitation Development in Narrow Cold-Frontal Rainbands., *J. Atmos. Sci.*,  
370 *41*, 2949–2972, doi:10.1175/1520-0469(1984)041;2949:TMAMSA;2.0.CO;2, 1984.

- 371 Schmitt, C. G., and A. J. Heymsfield, Observational quantification of the separation of  
372 simple and complex atmospheric ice particles, *Geophys. Res. Lett.*, pp. n/a–n/a, doi:  
373 10.1002/2013GL058781, 2014.
- 374 Schreur, B. W., and G. Geertsema, Theory for a TKE based parameterization of wind  
375 gusts, *HIRLAM Newsletter*, 54, pp. 177–188, 2008.
- 376 Seifert, A., and K. D. Beheng, A two-moment cloud microphysics parameterization for  
377 mixed-phase clouds. part 2: Maritime vs. continental deep convective storms, *Meteor.*  
378 *Atmos. Phys.*, 92(1-2), 67–82, doi:10.1007/s00703-005-0113-3, 2006.
- 379 Steenburgh, W. J., and T. I. Alcott, Secrets of the "Greatest Snow on Earth", *Bull. Amer.*  
380 *Meteorol. Soc.*, 89, 1285–1293, 2008.
- 381 Tao, W.-K., et al., Microphysics, radiation and surface processes in the goddard cumulus  
382 ensemble (gce) model, *Meteor. Atmos. Phys.*, 82(1), 97–137, 2003.
- 383 Thériault, J. M., R. Rasmussen, K. Ikeda, and S. Landolt, Dependence of snow gauge  
384 collection efficiency on snowflake characteristics, *J. Appl. Meteor. Climatol.*, 51, 745–  
385 762, doi:10.1175/JAMC-D-11-0116.1, 2012a.
- 386 Thériault, J. M., R. E. Stewart, and W. Henson, Impacts of terminal velocity on  
387 the trajectory of winter precipitation types, *Atmos. Res.*, 116(0), 116 – 129, doi:  
388 10.1016/j.atmosres.2012.03.008, jce:titlejRemote Sensing of Clouds and Aerosols: Tech-  
389 niques and Applications - Atmospheric Researchj/ce:titlej, 2012b.
- 390 Thompson, G., R. M. Rasmussen, and K. Manning, Explicit forecasts of win-  
391 ter precipitation using an improved bulk microphysics scheme. part i: Descrip-  
392 tion and sensitivity analysis, *Mon. Wea. Rev.*, 132(2), 519–542, doi:10.1175/1520-

393 0493(2004)132;0519:EFOWPU;2.0.CO;2, 2004.

394 Toloui, M., S. Riley, J. Hong, K. Howard, L. Chamorro, M. Guala, and J. Tucker, Measure-  
395 ment of atmospheric boundary layer based on super-large-scale particle image velocime-  
396 try using natural snowfall, *Experiments in Fluids*, 55(5), 1–14, doi:10.1007/s00348-014-  
397 1737-1, 2014.

398 Wakasugi, K., A. Mizutani, M. Matsuo, S. Fukao, and S. Kato, A direct method for  
399 deriving drop-size distribution and vertical air velocities from vhf doppler radar spectra,  
400 *J. Atmos. Oceanic Technol.*, 3(4), 623–629, 1986.

401 Wang, L.-P., and M. R. Maxey, Settling velocity and concentration distribution of heavy  
402 particles in homogeneous isotropic turbulence, *Journal of Fluid Mechanics*, 256, 27–68,  
403 doi:10.1017/S0022112093002708, 1993.

404 Yuter, S. E., D. E. Kingsmill, L. B. Nance, and M. Löffler-Mang, Observations of Precip-  
405 itation Size and Fall Speed Characteristics within Coexisting Rain and Wet Snow, *J.*  
406 *Appl. Meteorol. Clim.*, 45, 1450–1464, doi:10.1175/JAM2406.1, 2006.

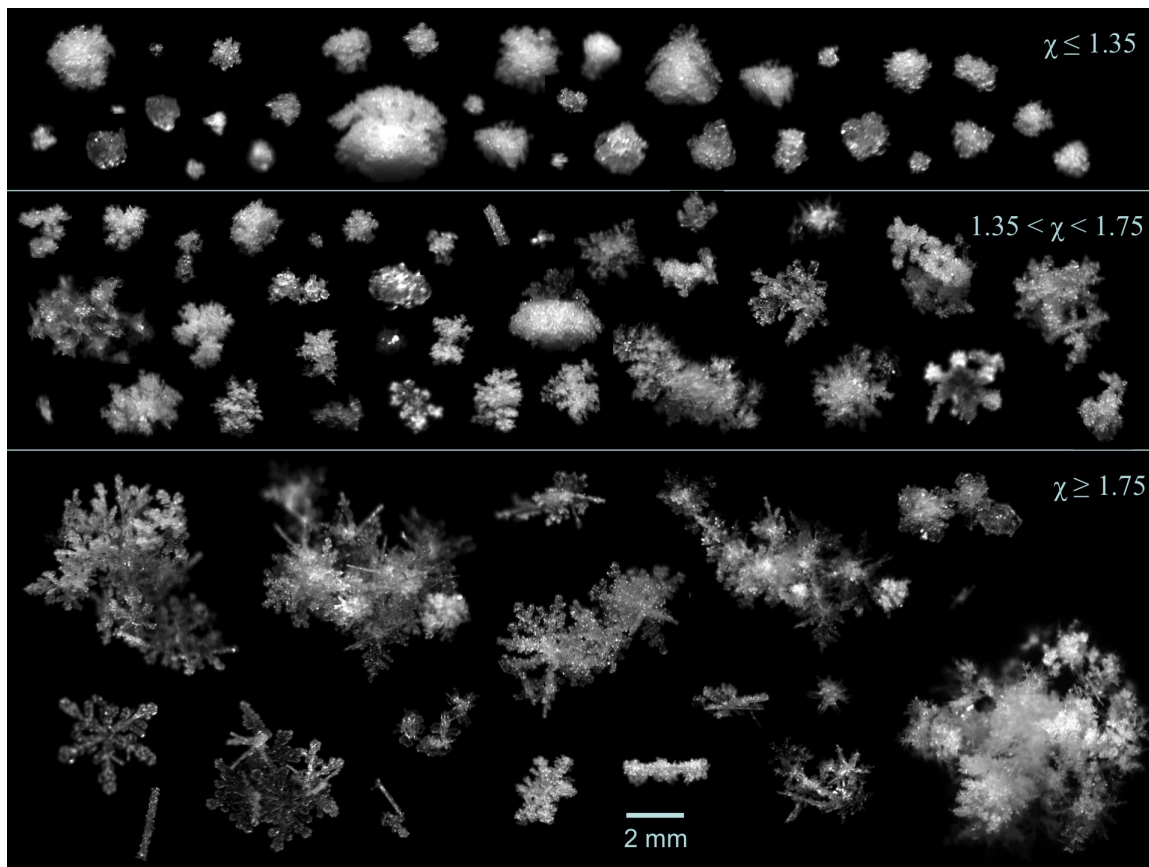


**Figure 1.** Images obtained from the center camera of the MASC during WASHARX categorized according to complexity  $\chi$  (Eq. 1). The pixel resolution is  $14 \mu\text{m}$ .

**Table 1.** Average values of complexity  $\chi$ , maximum dimension  $D_{max}$  (mm), slope parameter  $\lambda$  ( $\text{mm}^{-1}$ ), fallspeed  $v$  ( $\text{m s}^{-1}$ ), temperature at Baldy Summit  $T_{Baldy}$  and Alta Base  $T_{Base}$  ( $^{\circ}\text{C}$ ), radar echo depth  $H$  (km), and mean column values of radar echo  $Z$  (dBZ), Doppler spectral width  $SW$  ( $\text{m s}^{-1}$ ), and Doppler velocity  $v_D$   $\text{m s}^{-1}$ . Categories are as defined in the text. All quantity means are statistically different at the 95% confidence level using a Kolmogorov-Smirnov test.

Habit ( $N$ )	$\chi$	$D_{max}$	$\lambda$	$v$	$T_{Baldy}$	$T_{Base}$	$H$	$Z$	$SW$	$v_D$
Aggregates (9093)	2.00	3.6	0.69	0.72	-10.6	-4.3	1.34	7.2	0.52	0.80
Rimed (18924)	1.52	2.0	1.19	0.86	-10.3	-3.8	1.35	7.1	0.53	0.83
Graupel (7670)	1.29	1.4	1.99	0.90	-8.4	-2.1	1.27	7.2	0.62	0.93

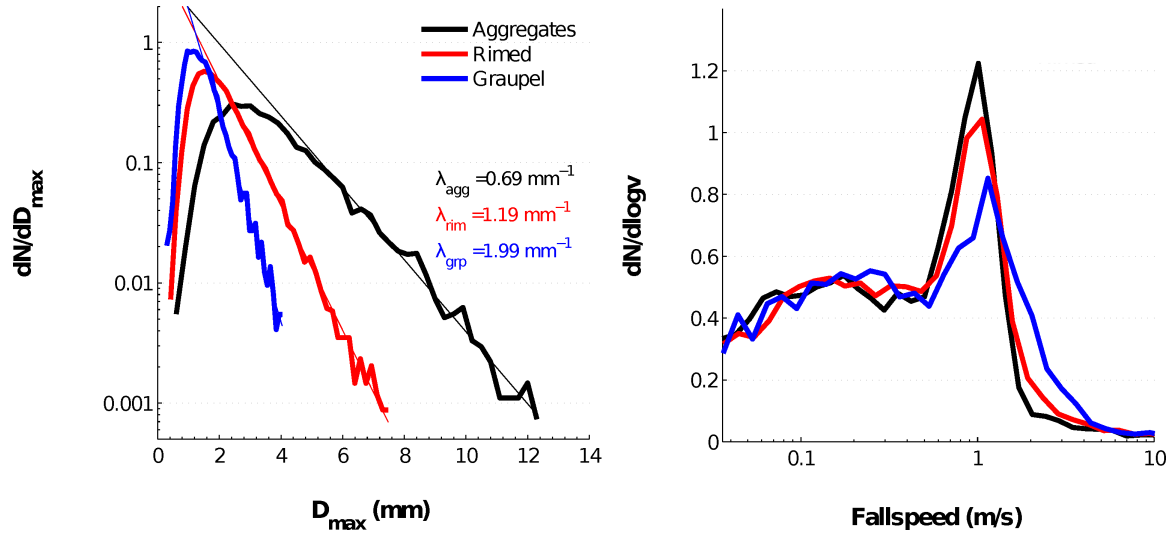


**Figure 2.** Distributions of maximum dimension  $D_{max}$  (left) and fallspeed  $v$  (right) obtained by the MASC during 2013, normalized to unity and categorized according to complexity  $\chi$  (Eq. 1). The parameter  $\lambda$  represents the slope of the tail of the distribution.

**Table 2.** As for Table 1, except *med* represents the median and  $\rho_g^{aer}$  represents the aerodynamically derived graupel density ( $\text{kg m}^{-3}$ ) using the expressions of *Böhm* [1989]. High and low refer to upper and lower quartiles bounded by  $-5^\circ \text{C}$  and  $-13^\circ \text{C}$  for Baldy summit temperature  $T$  and  $3.4 \text{ m}^2 \text{ s}^{-2}$  and  $0.4 \text{ m}^2 \text{ s}^{-2}$  for a local measure of turbulence near the MASC  $E$ . Quantities whose means are not statistically different at a 95% confidence level are italicized.

Graupel ( $N$ )	$\chi$	$D_{max}$	$v$	$v_{med}$	$\rho_g^{aer}$	$\rho_{gmed}^{aer}$	$T_{Baldy}$	$H$	$Z$	$SW$	$v_D$	$E$
$T_{high}$ (884)	1.18	<i>1.6</i>	1.16	0.56	217	44	<b>-3.5</b>	1.95	11.3	0.53	0.60	4.0
$T_{low}$ (1079)	1.20	<i>1.5</i>	0.70	0.31	159	19	<b>-17.3</b>	0.68	3.2	0.61	0.82	2.9
$E_{high}$ (3081)	1.18	<i>1.5</i>	0.93	0.33	208	22	-7.9	1.19	7.3	0.75	0.84	<b>8.1</b>
$E_{low}$ (555)	1.19	<i>1.5</i>	0.96	0.68	162	72	-8.4	1.80	9.0	0.48	0.83	<b>0.2</b>



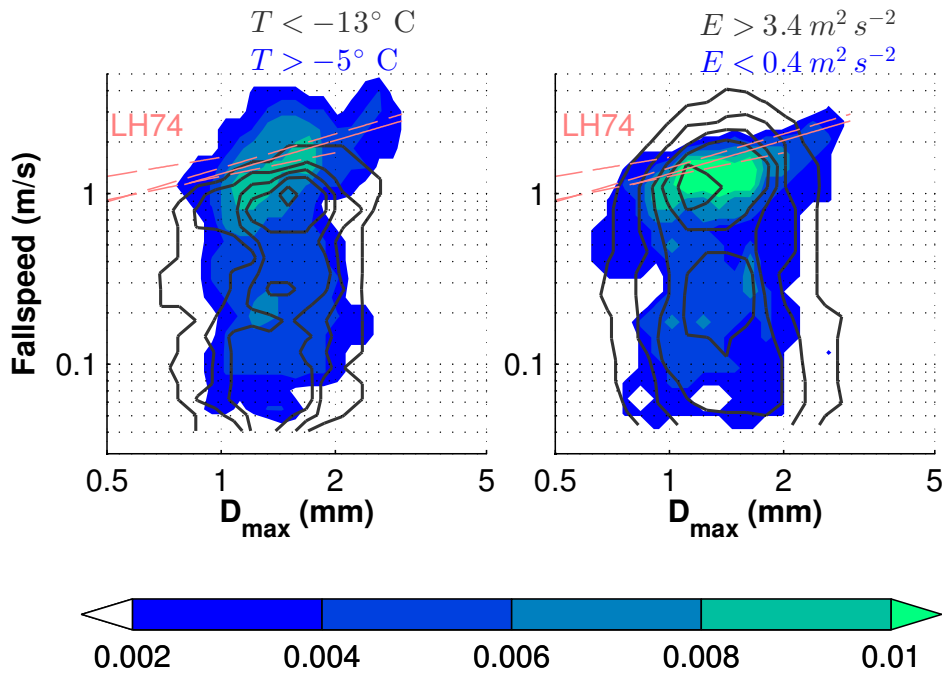


**Figure 3.** Normalized frequency distributions for graupel as a function of both fallspeed and graupel maximum dimension. Parameterized power-law relationships between fallspeed and maximum dimension for conical (solid) and three ranges of lump (dashed) graupel obtained by LH74, and adjusted to 2590 m AGL, are shown in red. Black, contoured isolines for high turbulence and low temperatures have equivalent spacing to the colored, filled isolines for low turbulence and high temperatures; the outer contour corresponds to the lowest frequency value of 0.002.